Biointerface Research in Applied Chemistry
Open-Access Journal (ISSN: 2069-5837)

Article
Volume 13, Issue 6, 2023, 547
https://doi.org/10.33263/BRIAC136.547

Structural and Spectroscopic Studies for Chitosan/Fe_3O_4 Nanocomposites as Glycine Biosensors

Taha M. Tiama [1], Asmaa M. Ismail [2], Hanan Elhaes [3], Medhat A. Ibrahim [2,*]

[1] Basic Science Department, October High Institute for Engineering & Technology, 6th October City, Cairo, Egypt
[2] Molecular Spectroscopy and Modeling Unit, Spectroscopy Department, National Research Centre, 33 El-Bohouth St., 12622, Dokki, Giza, Egypt
[3] Physics Department, Faculty of Women for Arts, Science, and Education, Ain Shams University, 11757 Cairo, Egypt
* Correspondence: medahmed6@yahoo.com (M.A.I.);

Scopus Author ID 8641587100
Received: 3.12.2022; Accepted: 5.01.2023; Published: 24.02.2023

Abstract: Owing to the unique properties of chitosan, composites of chitosan/Fe_3O_4 (0.25, 0.5, 0.75 wt. %) were cast, forming films, then subjected to different concentrations of glycine to be applied as a sensor for the amino acid. Prepared films were characterized using X-ray diffraction (XRD) and ATR-FTIR spectroscopy. Sensing performance was validated using UV-Vis spectroscopy. XRD data indicated that there are hydrogen bonds between Fe_3O_4 and chitosan structure. The interaction between chitosan and magnetite (Fe_3O_4) could be described as a composite in the same matrix. ATR-FTIR spectra demonstrated the broadening of chitosan/Fe_3O_4 bands in the range of 3360-3041 cm^{-1}, as well as an increase in the intensity of the bands at 1638, 1564, 1151, and 704 cm-1 with the addition of Fe_3O_4 associated with a shift of the band at 2987 cm^{-1} toward lower wavenumber, indicating that Fe_3O_4 is embedded and interacted with chitosan. The shift of band positions of functional groups to lower wavenumber can be interpreted as the strengthening of the chemical bonds due to molecular adsorption. UV-Vis results indicated that chitosan/ Fe_3O_4 0.25 wt % ratio had the best sensitivity compared to pure chitosan and other chitosan/ Fe_3O_4 ratios. Correlating the data, it can be concluded that chitosan/Fe_3O_4 could act as a biosensor for the amino acid glycine.

Keywords: chitosan/Fe_3O_4; glycine; biosensor; XRD; UV-Vis; ATR-FTIR.

1. Introduction

Polymer blends incorporated with nanoparticles (NPs) are now widely applied owing to their enhanced physical, chemical, and biological properties [1-3]. Chitosan and other biopolymers show unique hydrogen bonding [4, 5]. It was reported that chitosan could be modified with nanometal oxide to enhance its ability for further applications [6-8]. In order to investigate the effect of metal oxide on the electronic properties and, subsequently, the functionality, molecular modeling is consulted. Using molecular modeling calculations, chitosan was enhanced with graphene and then successfully applied to remove heavy metals from wastewater [9, 10]. Based on theoretical and experimental results, it was stated earlier that nano metal oxide such as TiO_2 enhanced the ability of nano chitosan blend to act as biosensors for amino acids [11]. The analyses of modeling data indicated that the presence of metal oxide is changing the electronic properties by decreasing the value of HOMO/LUMO band gap energy and increasing the total dipole moment (TDM). Earlier, the reactivity of a given structure was correlated with physical properties such as HOMO/LUMO and TDM [12,

13]. The unique electronic properties of chitosan and other biopolymers enhanced with nanometal oxide pave the way toward applying metal oxide-enhanced biopolymers as sensors owing to their biodegradability, easy handling, and low cost [14- 16]. The application of molecular bioelectronics has allowed the production of highly responsive biosensors to detect various analytics of interest [17]. Because of their possible applications in biomedical research, and environmental and biotechnology analyses, biosensors have attracted much attention. Different factors, such as electrode material and morphology, are involved in applying a biosensor and its compatibility with biosensing molecules [18]. Chitosan is one of the most widely used natural polymers to disperse nanomaterials due to its excellent properties, such as good film formation, biocompatibility, non-toxicity, mechanical strength, and water permeability. Chitosan can adsorb negatively charged material or bind to a surface with negative charges when dissolved and introduced with its positively charged NH_3^+ group. The composition of the primary NH_2 group helps in grafting the chitosan chain with nanomaterials, leads to good dispersion of nanomaterials, and forms stable chitosan nanocomposite materials [19]. Due to their low toxicity and superparamagnetic activity, magnetic NPs such as Fe_3O_4 have shown tremendous potential for various applications such as wastewater treatment, enzyme immobilization, biosensors, and drug delivery applications [20, 21]. This magnetic material possesses significant advantages, including the high specific surface area, which enhances its binding performance, low resistance to mass transfer, decreased error and selective separation under a magnetic field of the immobilized enzymes, and, thus, lower operating costs [22]. However, Fe_3O_4 NPs have a high surface area-to-volume ratio of high surface energy and appear to accumulate, reducing their range of applications [23, 24].

Fe_3O_4 NPs are dedicated to many applications based on their unique physical, chemical, and surface properties [25-28]

Preparation of chitosan/Fe_3O_4 NPs using the casting method provides a simple method for preparing polymer/nanocomposite films with good properties. In addition, this polyaminosaccharide has specific chemical properties that allow the formation of positively charged complexes through its free amino groups, creating reactive sites to attach Fe-based NPs [29, 30]. Recently, chitosan/Fe_3O_4 nanocomposite was effectively and safely applied as a catalyst [31]. Based on its catalytic activity, it was used with sodium alginate and ZnO to remove pharmaceuticals [32,33] efficiently. A mixture of chitosan with Fe_3O_4 NPs was reported to improve the oxidation current in gallic acid (GA) and is used for electrochemical studies and the determination of (GA) [34]. Chitosan could be coated with Fe_3O_4 and subjected to different characterizations [35].

Further enhancement for such nanocomposite is conducted with graphene quantum dots to act as a magnetic imaging agent [36]. Chitosan-agarose is functionalized with core-shell type Fe_3O_4 to act as an anticancer against liver and lung cancer cells [37]. Many researchers reported that chitosan/iron oxide show application efficient green catalyst [38]. It also could act as an active photocatalytic removing agent [39]. It also could be applied for the possible removal of dye and mercury from wastewater [40].

Based on the above considerations, chitosan could be enhanced for application as a biosensor. Accordingly, the present work is conducted to study the structural and optical properties of chitosan and chitosan/Fe_3O_4 nanocomposites with different weight percentages using XRD, ATR-FTIR spectroscopy, and UV-Vis spectroscopy to assess their performance as a biosensor for amino acid glycine and to determine the best ratio for this purpose.

2. Materials and Methods

2.1. Materials.

Medium molecular weight chitosan was supplied from Sigma-Aldrich. Ferrous sulfate ($FeSO_4.7H_2O$) Extra pure was purchased from Sham Lab, and Ferric chloride ($FeCl_3.5H_2O$) was supplied from Laboratory Rasayan (LR). Ammonium hydroxide solution (NH_4OH) was purchased from AbcoChemie, England, an assay of 25% NH_3 (AR). Acetic acid was purchased from Merck Company, and glycine was purchased from Adwic Company.

2.2. Preparation of Fe_3O_4.

Fe_3O_4 NPs were synthesized using the co-precipitation method. At 70ºC, $FeSO_4.7H_2O$ and $FeCl_3.6H_2O$ (Fe^{2+} and Fe^{3+}) with a molar ratio 2:1, respectively, were dissolved separately in distilled water. After that, both solutions were mixed under continuous stirring. The final pH of the solution was adjusted to 10 using NH_4OH. A dark precipitate was formed and finally left to dry at 50ºC for 24 hrs.

2.3. Preparation of chitosan/Fe_3O_4 polymer nanocomposite.

An appropriate weight of chitosan was dissolved in 98 ml of DI water and 2 ml of acetic acid under continuous stirring at 60ºC for 4 hrs, until a homogenous viscous solution was formed. Different weight percentages of Fe_3O_4 (0.25, 0.5, 0.75 wt%) were added to the chitosan solution. The solution is magnetically stirred for 6 hrs, then sonicated using Hielscher UP100H ultrasonic for 1 hr to prevent agglomeration of the NPs. The nanocomposite solutions were cast in plastic Petri dishes and dried at 40ºC for 24 hrs. The resulting films were approximately 20 μm in thickness.

2.4. Sensing experiment.

A 1M glycine solution was prepared and then diluted into 10^{-1}, 10^{-2}, 10^{-3}, and 10^{-4} M solutions. Next, each nanocomposite film was cut into stripes (0.5 x 3 cm), and stripes were dipped into the four different concentrations of glycine solution for 60 seconds to choose the optimum ratio that could be used as a biosensor for glycine.

2.5. Characterization techniques.

X-ray diffraction (XRD) in the 2θ range of (5°–80°) is performed using PANalyticalX'Pert Pro target Cu-Kα with secondary monochromator Holland radiation with tube operating at 45 kV and wavelength of 0.1540 nm.

Attenuated total reflection infrared (ATR-FTIR) spectra were obtained in the mid-infrared spectral range of 4000-400 cm^{-1} with a resolution of 4 cm^{-1}, using VERTEX 80 FTIR spectrometer from Bruker Optik GmbH, Germany, equipped with platinum diamond ATR crystal system, which consists of a diamond disc as an internal reflection element.

Ultraviolet-visible absorption spectra were obtained in the 200-1000 nm wavelength range using a V-630 UV-Vis spectrophotometer (Jasco).

3. Results and Discussion

3.1. X-ray diffraction (XRD).

Figure 1 shows XRD patterns of chitosan and Fe_3O_4. XRD pattern of chitosan shown in Figure 1-a demonstrated weak diffraction peaks at 2θ = 9° and 12° which are assigned to chitosan's crystal form I, and a strong, broad peak at 2θ = 20° which is assigned to chitosan's crystal form II, and is attributed to the amorphous nature of the chitosan. The crystalline forms are due to the nature of the crystallinity of chitosan [34]. Because of hydrogen bonds between the amino and hydroxyl groups, and the regularity of the chitosan structure, no impurities were observed, indicating the high purity of chitosan [41-44]. Figure 1-b shows the crystalline diffraction peaks for Fe_3O_4 of 2θ values at 18.4°, 30.19°, 35.55°, 43.03°, 57.17°, 62.74° and 74.3° which agree the results previously reported in the literature [45].The average crystal size of Fe_3O_4 can be calculated using the Scherrer equation [46]:

$$D = {K\lambda}/{\beta cos\theta} \quad (1)$$

where D is the size of the crystal, k is a constant (0.915), λ is the wavelength of the X-ray (0.154 nm), β is the full width at half maximum (FWHM) of the diffraction peak (in radian), and θ (in degrees) is the Bragg's diffraction angle of the maximum peak. The average crystal size of Fe_3O_4 was found to be 5 nm. Hence, we found that the surface-to-volume ratios are high, which results in increased surface reaction activity, catalytic efficiency, and strong absorption.

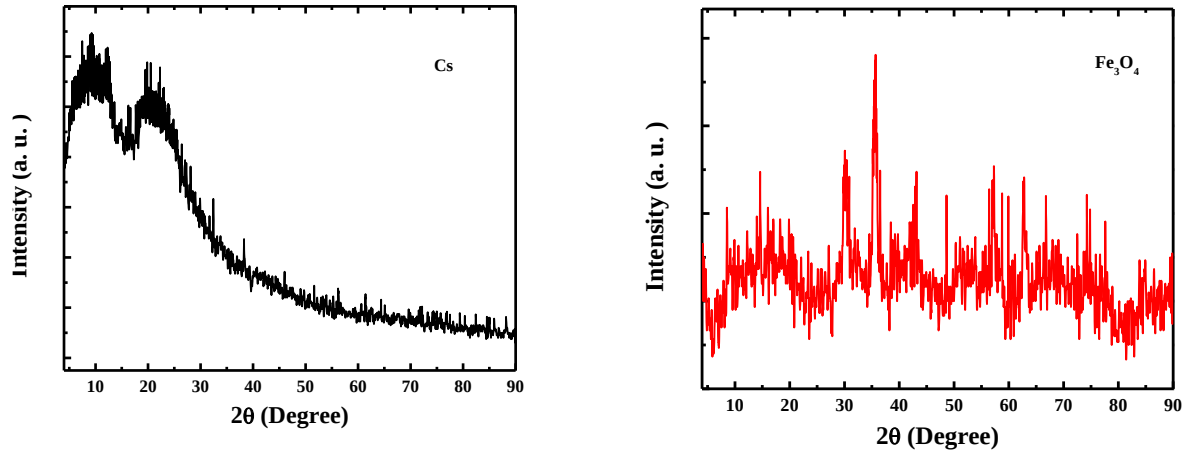

(a) (b)

Figure 1. XRD patterns of **(a)** Chitosan and **(b)** Fe_3O_4.

Figure 2 shows XRD patterns for chitosan and chitosan/Fe_3O_4 with different weight percentages of Fe_3O_4. As demonstrated in the Figure, the intensities of the diffraction peaks of 2θ values at 9° and 12° increased with the addition of Fe_3O_4 but became less broad when compared to pure chitosan. This finding indicates the change in the regularity of chitosan chains resulting from the interaction of chitosan with Fe_3O_4. In addition, the diffraction peak at 2θ of 20°became broader and shifted toward a higher 2θ degree, while the characteristic peaks of Fe_3O_4 disappeared. These results confirm the interaction between chitosan and Fe3O4 and their complex formation. The results show that the proposed preparation method resulted in chitosan incorporated with Fe_3O_4 as a composite in the same matrix, which agrees with what was previously reported in the literature [47].

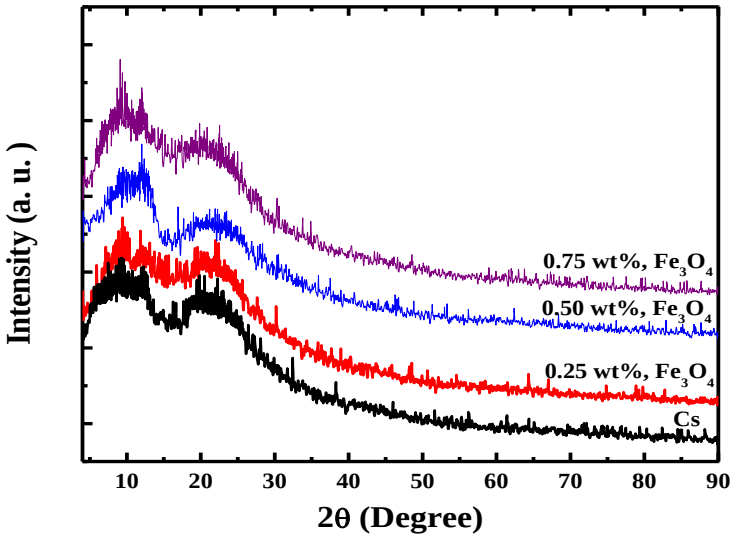

Figure 2. XRD patterns of chitosan and chitosan/Fe_3O_4 with a different weight percentage of Fe_3O_4.

3.1.1. ATR-FTIR spectroscopy.

Figure 3 shows the ATR-FTIR spectra of chitosan, Fe_3O_4, and chitosan/Fe_3O_4 nanocomposites with the different weight percentages of Fe_3O_4 (0.25, 0.5, and 0.75 wt%). As shown in Figure 3-a, chitosan has two bands at 3337 cm^{-1} and 3257 cm^{-1}, characteristic of the stretching vibrations of O-H and N-H, respectively.

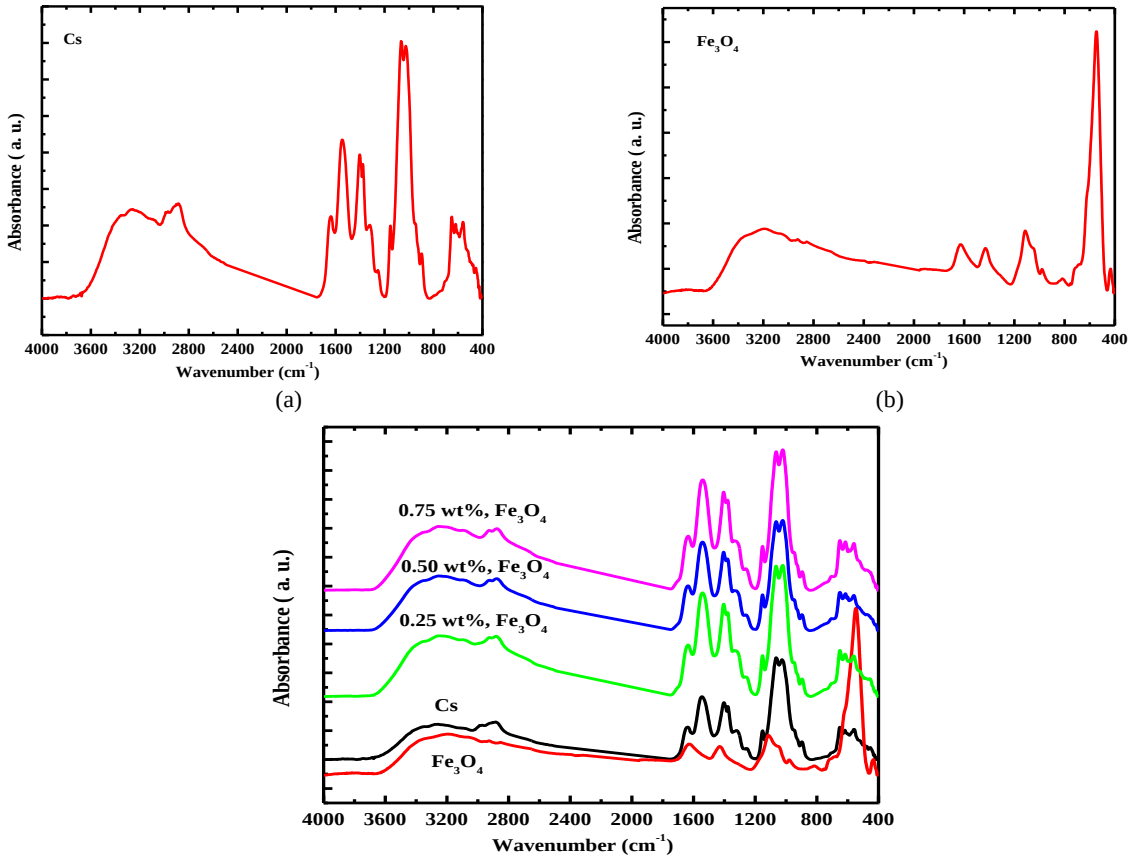

Figure 3. ATR-FTIR spectra of **(a)** Chitosan, **(b)** Fe_3O_4, and **(c)** Chitosan/Fe_3O_4 with a different weight percentage of Fe_3O_4.

The symmetric and asymmetric vibrations of C-H stretching vibration are observed at 2987 cm^{-1} and 2883 cm^{-1}, respectively. The presence of bands affirms the residual of N-acetyl groups at 1638 cm^{-1}, which is assigned to C=O stretching vibration of amide I, 1564 cm^{-1}, which is attributed to bending vibration of N-H group (amide II) and 1321 cm^{-1} that related to stretching vibration of C-N group (amide III). The bending vibration of CH_2 and symmetrical deformation of CH_3 are noted at 1402 cm^{-1} and 1377 cm^{-1}, respectively. The band at 1151 cm^{-1} corresponds to the asymmetric stretching vibration of the C-O-C bridge [48]. The stretching vibrations of the C-O group of β (1→4) glycosidic bonds are observed at 1064 cm^{-1}, 1026 cm^{-1}, and 897 cm^{-1}. The band at 650 cm^{-1} is related to the bending vibration of the O-H group [49, 50]. From Figure 3-b, Fe_3O_4 shows bands at 3193 cm^{-1} and 1630 cm^{-1} corresponding to the stretching and bending vibration of the O-H group of moisture. The strong band at 546 cm^{-1} corresponds to Fe-O vibration [51].

Figure 3-c presents the ATR-FTIR of chitosan, Fe_3O_4, and chitosan/Fe_3O_4 with different weight percentages of Fe_3O_4. From the Figure, the bands in the range of 3360-3041 cm^{-1} become broader. A new band appeared at 593 cm^{-1}, and the intensities of the bands at 1638 cm^{-1}, 1564 cm^{-1}, 1151 cm^{-1}, and 704 cm^{-1} increased and shifted to lower frequencies with the addition of Fe_3O_4. In addition, the band at 2987 cm^{-1} shifted toward a lower frequency. These results confirm that Fe_3O_4 is embedded in and interacts with chitosan.

3.1.2. Optical properties.

UV-Vis spectra of chitosan and chitosan/Fe_3O_4 with different weight percentages of Fe_3O_4 are shown in Figure 4. Chitosan shows a peak at 217 nm and a broad hump at 341 nm which are attributed to л-л* and n-л* inter-band transitions, respectively [52]. After the addition of Fe_3O_4 with different weight percentages, the peak at 217 nm is shifted to a lower wavelength, 213 nm (blue shift), and the hump at 341 nm decreased in intensity and became faint with the addition of Fe_3O_4, and this indicates the complexation and interaction between chitosan and Fe_3O_4.

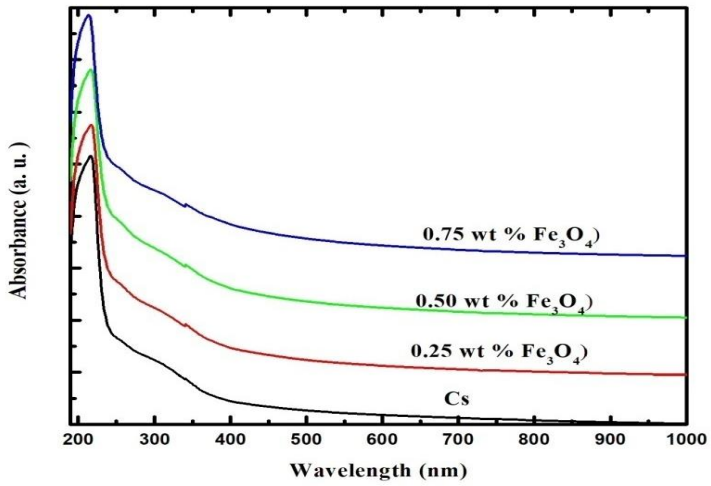

Figure 4. UV-Vis spectra of chitosan and chitosan/Fe_3O_4 with a different weight percentage of Fe_3O_4 (0.25, 0.5, and 0.75 wt%).

One of the fundamental parameters that depend on the wavelength of the incident light and gives detailed data on the attenuation of the intensity of the incident light by the studied samples is the optical absorption coefficient (α). This coefficient can be determined from the absorbance (A) and thickness of the sample (T) using the Swapole formula [53]:

$$\alpha(\lambda) = \frac{2.303}{T} A \quad (2)$$

Figure 5 shows the relation between the calculated α and the photon energy (hυ) for all the studied samples. The absorption edge values can be estimated by extrapolating the linear portions of the α curve to zero absorption values.

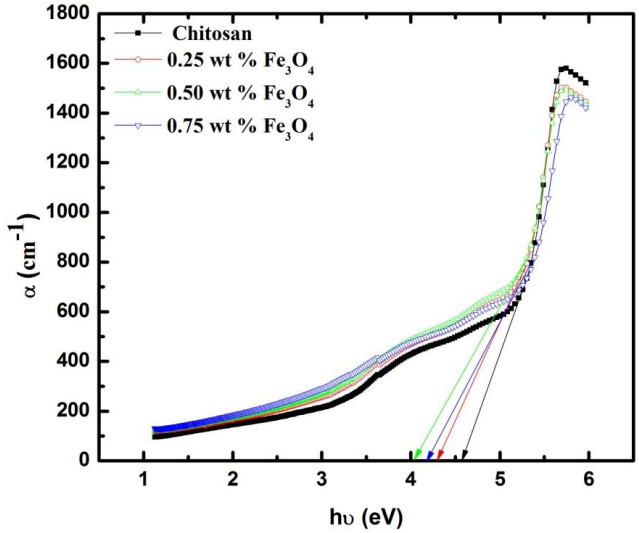

Figure 5. Relation between α and hυ for chitosan and chitosan/Fe_3O_4 with a different weight percentage of Fe_3O_4 (0.25, 0.5, and 0.75 wt%).

Table 1 presents the calculated values of absorption edge, band tail energy, direct energy gap, and indirect energy gap (Egi) for chitosan and chitosan/Fe_3O_4 nanocomposites with different weight percentages Fe_3O_4 which were obtained from optical absorption coefficient. As seen in table 1, the absorption edge values are shifted to lower photon energy. This means there is a change in the band structure of chitosan, and there is a structural disorder resulting from adding Fe_3O_4.

The structure of polymeric materials can be investigated using Urbach energy by detecting the defect level and measuring the degree of disordering in the forbidden band gap [54]. The width of the tail was estimated through the following relation:

$$\alpha = \alpha_0 \exp\left(\frac{h\upsilon}{E_t}\right) \quad (3)$$

where α_0 is a constant and Et is band tail energy.

Figure 6 shows the relation between lnα and hυ. The reciprocal of the slope of the curve gives the value of band tail energy. Values of band tail energy are increased by adding Fe_3O_4.

As seen in table 1, band tail energy values are increased by adding Fe_3O_4, which indicates the high density of the localized tail states and causes the tail-to-tail transitions. Additionally, the characteristic change in the optical properties causes disorder in the polymer composite system due to the intermolecular interaction between the blend components and Fe_3O_4.

Measuring band gap energy is an important parameter for determining the optical transition in any material. The nature of electronic transition (μ) in any material is classified according to band gap into direct and indirect band gaps. In a direct band gap, μ=2 when the maximum of the valance band and the minimum of the conduction band coexist at the same momentum point of the zero crystal (k (wave vector) = 0).

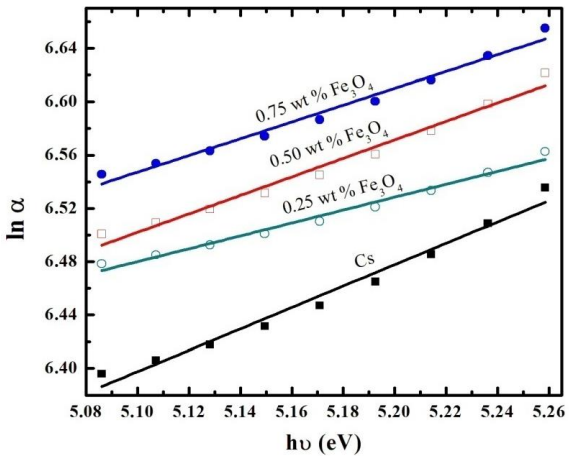

Figure 6. Relation between lnα and hυ for chitosan and chitosan/Fe_3O_4 with a different weight percentage of Fe_3O_4 (0.25, 0.5, and 0.75 wt%).

For indirect band gap, μ=1/2 when the valence band's maximum and the conduction band's minimum do not lie at the same wave vector. The absorption of the phonon energy will often be correlated with the right crystal momentum magnitude of the electron transfer from the valence band to the conduction band. The optical band gap energy is calculated using Mott and Davis method [55]:

$$(\alpha h\upsilon) = B\,(h\upsilon - Eg)1/\mu \qquad (4)$$

where B is the probability of transition.

Figure 7 shows the relation between (αhυ)2 and (αhυ)1/2 against hυ for chitosan and chitosan/Fe_3O_4 with 0.25, 0.5, and 0.75 wt% of Fe_3O_4. The values of direct and indirect band gap energy are determined from the extrapolation of the linear portions of (αhυ)2 and (αhυ)1/2 curves to zero absorption values. E.g., the value demonstrated the electronic transition between the highest occupied molecular orbital (HOMO) and the lowest unoccupied molecular orbital (LUMO).

Table 1. Values of absorption edge as (eV), band tail energy, direct energy gap (E_{gd}) as (eV), and indirect energy gap (E_{gi}) as (eV) for chitosan and chitosan/Fe_3O_4 with a different weight percentage of Fe_3O_4.

Samples	Absorption edge(eV)	Band tail energy (eV)	Energy gap (eV)	
			E_{gd}	E_{gi}
Chitosan	4.55	1.25	3.71	2.21
Chitosan/0.25 wt% Fe_3O_4	4.29	1.44	3.29	1.84
Chitosan/0. 5 wt% Fe_3O_4	4.04	1.59	3.01	0.84
Chitosan/0.75 wt% Fe_3O_4	4.17	2.06	3.17	1.81

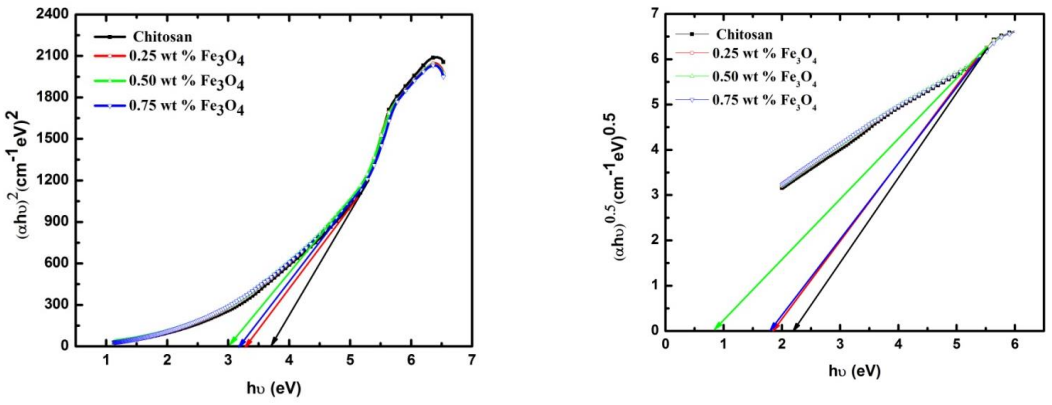

(a) (b)

Figure 7. Relation between $(\alpha h\upsilon)^{0.5}$ and $(\alpha h\upsilon)^2$ versus hυ for chitosan and chitosan doped with 0.25, 0.5, and 0.75 wt% magnetite Fe_3O_4.

As seen in Table 1, the band gap energy values decreased with adding Fe_3O_4. This confirmed that adding Fe_3O_4 creates localized states, causes defects in chitosan structure, and increases the degree of disorder of the system.

UV–Vis spectroscopy was also used to monitor the studied nanocomposite samples' performance as a glycine sensor. Figure 8 shows the absorbance of 10^{-1}, 10^{-2}, 10^{-3}, and 10^{-4} M glycine solutions after dipping stripes of chitosan and chitosan/Fe_3O_4 with different concentrations of Fe_3O_4 for 60 seconds. As seen from the Figure, the absorbance of the studied samples is increased with increasing glycine concentration and shifted toward a longer wavelength. This may be attributed to the increased pH values of the prepared solutions. In addition, there are noticeable changes in the absorbance of all samples with different glycine concentrations. These changes in absorbance are attributed to the interaction between the carboxylic group of glycine and functional groups of chitosan (N-H and O-H) and Fe_3O_4, as indicated earlier [11].

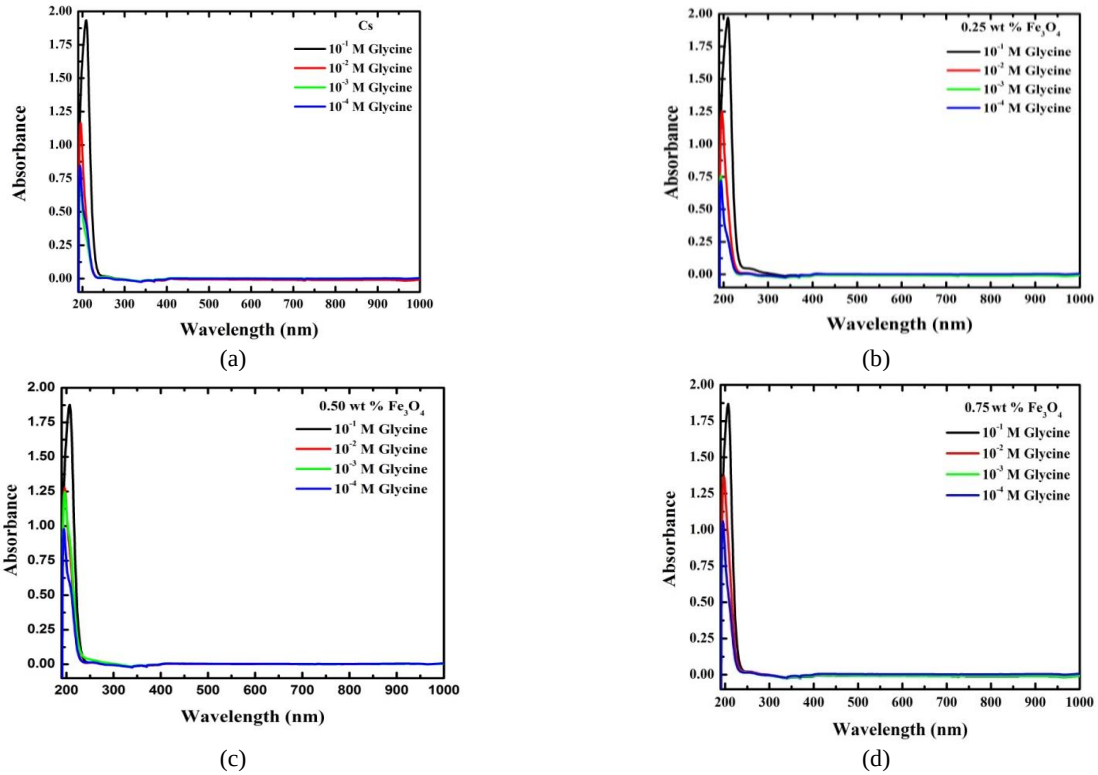

Figure 8. UV–Vis absorption spectra for the glycine after exposure to **(a)** chitosan and chitosan/Fe_3O_4 with different weight percentages of Fe_3O_4 **(b)** 0.25 wt% Fe_3O_4, **(c)** 0.5 wt% Fe_3O_4 and **(d)** 0.75 wt% Fe_3O_4 for insertion time 60 sec.

Figure 9 shows the UV–Vis absorption spectra for glycine concentration 10-4 M after exposure to chitosan and chitosan/Fe_3O_4 with different weight percentages of Fe_3O_4. As seen in Figure 9, chitosan/Fe_3O_4 nanocomposite containing 0.25 wt% of Fe_3O_4 showed better sensitivity than pure chitosan and chitosan/Fe_3O_4 with other wt%, and this concentration can be used as a biosensor for glycine. In addition, shifts of band peak positions of the molecular functional groups to higher wavelength values were noticed and can be interpreted as strengthening the chemical bonds of these functional groups due to molecular adsorption. These results suggest that these features could enable chitosan with a nanometal oxide like Fe_3O_4 to be used in new signal transmission techniques in biosensors for rapid in vivo analysis. As the reported literature shows, this is because the dynamic interface properties are based on surface charge and effective area, roughness, porosity, functional groups, energy and

valence/conduction states, and the hygroscopic nature of nano metal oxide [56]. The association of biomolecules with nanometal oxide can be achieved through physical adsorption or chemical bonding. This interconnection between biomolecules depends on the availability of functional groups, which can be formed through appropriate chemical reactions. In contrast, the physical adsorption of the biomolecules arises mainly from weak interactions (for example. Decomposition, Van Der Waals, electricity) [57].

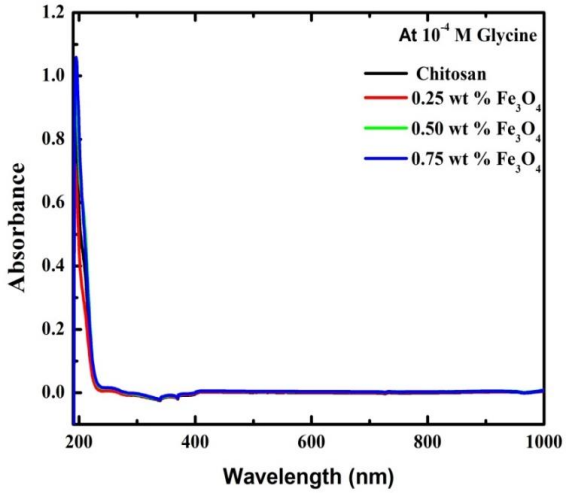

Figure 9. UV–Vis absorption spectra for the glycine concentration 10^{-4} M after exposure to chitosan and chitosan/Fe_3O_4 with a different weight percentage of Fe_3O_4 (0.25, 0.5, and 0.75 wt%) for insertion time 60 sec.

4. Conclusions

The casting technique prepared a nanocomposite of chitosan/Fe3O4 (0.25, 0.5, 0.75 wt%). Samples were subjected to 10^{-1}, 10^{-2}, 10^{-3}, and 10^{-4} M glycine solutions for an insertion time 60 seconds to identify use the optimal ratio that gives the best sensitivity to be used as a biosensor for glycine. XRD, ATR-FTIR, and UV-Vis spectroscopy were used to investigate the effect of adding different concentrations of Fe_3O_4 to chitosan. XRD and ATR-FTIR techniques confirmed the complexity and interaction between chitosan and Fe_3O_4. The size of Fe_3O_4 was found to be 5 nm using the Scherrer equation. UV-Vis absorption spectra demonstrated a blue shift of the peak at 217 nm, confirming the interaction between chitosan and Fe_3O_4. Values of absorption edge, band tails, and direct and indirect band gaps confirmed the creation of localized states between electronic transitions, thus causing defects in chitosan structure and increasing the degree of disorder. It was found that chitosan with 0.25 wt% of Fe_3O_4 showed the best sensitivity to glycine solutions compared to pure chitosan and other samples. This ratio between chitosan and Fe_3O_4 can be used as a biosensor for glycine amino acids.

Funding

We receive no funding for this work.

Acknowledgments

We would like to express our deep thanks to the members of the Molecular Spectroscopy and Modeling Unit at Spectroscopy Department, National Research Centre, Egypt, for their kind support during this work.

Conflicts of Interest

The authors declare no conflict of interest.

References

1. Barakat, N. A.; Taha, A.; Motlak, M.; Nassar, M. M.; Mahmoud, M. S.; Al-Deyab, S. S; ElNewehy, M.; Kim, H. Y. ZnO&Fe_2O_3-incoportaed TiO_2 nanofibers as super effective photocatalyst for water splitting under visible light radiation. *Appl. Catal. A: Gen.* **2014**, *481*, 19-26, http://dx.doi.org/10.1016/j.apcata.2014.04.045.
2. Barakat, N. A.; Ahmed, E.; Abdelkareem, M. A.; Farghali, A. A.; Nassar, M. M.; El-Newehy, M. H.; Al-Deyab, S. S. Ag, Zn and Cd-doped titanium oxide nanofibers as effective photocatalysts for hydrogen extraction from ammonium phosphates. *J. Mol. Catal.* **2015,** *409*, 117-126, http://dx.doi.org/10.1016/j.molcata.2015.08.015.
3. Ghouri, Z. K.; Al-Meer, S.; Barakat, N. A.; Kim, H. Y. ZnO@ C (core@ shell) microspheres derived from spent coffee grounds as applicable non-precious electrode material for DMFCs. *Sci. Rep.* **2017,** *7*, 1-8, https://doi.org/10.1038/s41598-017-01463-3.
4. Brown, E. E.; Laborie, M. P. G.; Zhang, J. Glutaraldehyde treatment of bacterial cellulose/fibrin composites: impact on morphology, tensile and viscoelastic properties. *Cellulose* **2012,** *19*, 127-137, http://dx.doi.org/10.1007/s10570-011-9617-9.
5. Fatullayeva, S.; Tagiyev, D.; Zeynalov, N.; Mammadova S.; Aliyeva E. Recent advances of chitosan-based polymers in biomedical applications and environmental protection. *J. Polym. Res.* **2022,** *29*, 259, https://doi.org/10.1007/s10965-022-03121-3.
6. Latif, U.; Al-Rubeaan, K.; Saeb, A. T. A review on antimicrobial chitosan-silver nanocomposites: a roadmap toward pathogen targeted synthesis. *Int. J. Polym. Mater. Polym.* **2015**, *64*, 448-458, https://doi.org/10.1080/00914037.2014.958834.
7. Morsi, R. E.; Alsabagh, A. M.; Nasr, S. A.; Zaki, M. M. Multifunctional nanocomposites of chitosan, silver nanoparticles, copper nanoparticles and carbon nanotubes for water treatment: antimicrobial characteristics. *Int. J. Biol. Macromol.* **2017,** *97*, 264-269, https://doi.org/10.1016/j.ijbiomac.2017.01.032.
8. Singh Dhillon, G.; Kaur, S.; Jyoti Sarma, S.; Kaur Brar, S.; Verma, M.; Surampalli, R. Y. Recent development in applications of important biopolymer chitosan in biomedicine, pharmaceuticals and personal care products. *Curr. Tissue Eng.* **2013**, *2*, 20-40, http://dx.doi.org/10.2174/2211542011302010004.
9. Ezzat, H.; Menazea, A. A.; Omara, W.; Basyouni, O. H.; Helmy, S. A.; Mohamed, A. A.; Tawfik. W.; Ibrahim, M. DFT: B3LYP/LANL2DZ Study for the Removal of Fe, Ni, Cu, As, Cd and Pb with Chitosan. *Biointerface Res. Appl. Chem.* **2020** *10*, 7002-7010, https://doi.org/10.33263/BRIAC106.70027010.
10. Menazea, A. A.; Ezzat, H. A.; Omara, W.; Basyouni, O. H.; Ibrahim, S. A.; Mohamed, A. A.; Tawfik. W.; Ibrahim, M. A. Chitosan/graphene oxide composite as an effective removal of Ni, Cu, As, Cd and Pb from wastewater. *Comput. Theor. Chem.* **2020,** *1189*, 112980,. https://doi.org/10.1016/j.comptc.2020.112980.
11. Ibrahim, M.; Mahmoud, A. A.; Osman, O.; Refaat, A.; El-Sayed, E. S. M. Molecular spectroscopic analysis of nano-chitosan blend as biosensor. *Spectrochim. Acta A Mol. Biomol. Spectrosc.* **2010,** *77*, 802-806, https://doi.org/10.1016/j.saa.2010.08.007.
12. Omar, A.; Badry, R.; Hegazy, M. A.; Yahia, I. S.; Elhaes, H.; Zahran, H.Y.; Ibrahim, M. A.; Refaat, A. Enhancing the Optical Properties of Chitosan, Carboxymethyl Cellulose, Sodium Alginate Modified with Nano Metal Oxide and Graphene Oxide. *Optical and Quantum Electronics* **2022,** *54*, 1-15, https://doi.org/10.21203/rs.3.rs-1079643/v1.
13. Ebied, M.S.; Dongol, M.; Ibrahim, M.; Nassary, M.M.; Elnobi, S.; Abuelwafa, A. A.; Structural and Optical Properties of Nanocrystalline 3-(2-Benzothiazolyl)-7-(diethylamino) Coumarin (C6) Thin Films for Optoelectronic Application. *J. Electron. Mater*. **2022**, *51*, 5770–5782, https://doi.org/10.1007/s11664-022-09792-4.
14. Ali, F. I.; Mahmoud, S. T.; Awwad, F.; Greish, Y. E.; Abu-Hani, A. F. Low power consumption and fast response H2S gas sensor based on a chitosan-CuO hybrid nanocomposite thin film. *Carbohydr. Polym.* **2020**, *236*, 116064., https://doi.org/10.1016/j.carbpol.2020.116064.
15. Chen, T. W.; Chinnapaiyan, S.; Chen, S. M.; Ali, M. A.; Elshikh, M. S.; Mahmoud, A. H. Facile synthesis of copper ferrite nanoparticles with chitosan composite for high-performance electrochemical sensor. *Ultrason Sonochem.* **2020,** *63*, 104902, https://doi.org/10.1016/j.ultsonch.2019.104902.
16. Adnan, M. A. M.; Phoon, B. L.; Julkapli, N. M. Mitigation of pollutants by chitosan/metallic oxide photocatalyst: a review. *J. Clean. Prod.* **2020**, *261*, 121190, https://doi.org/10.1016/j.jclepro.2020.121190.
17. Singh, A.; Sinsinbar, G.; Choudhary, M.; Kumar, V.; Pasricha, R.; Verma, H. N.; Pasricha. R.; Arora, K. Graphene oxide-chitosan nanocomposite based electrochemical DNA biosensor for detection of typhoid. *Sens. Actuators B Chem.* **2013,** *185*, 675-684, https://doi.org/10.1016/j.snb.2013.05.014.

18. Yu, H.; Guo, W.; Lu, X.; Xu, H.; Yang, Q.; Tan, J.; Zhang, W.; Reduced graphene oxide nanocomposite based electrochemical biosensors for monitoring foodborne pathogenic bacteria: A review, *Food Control* **2021**, *127*, 108117, https://doi.org/10.1016/j.foodcont.2021.108117.
19. Mohammed, M. A.; Syeda, J.; Wasan, K. M.; Wasan, E. K. An overview of chitosan nanoparticles and its application in non-parenteral drug delivery. *Pharmaceutics* **2017,** *9*, 53, https://pubmed.ncbi.nlm.nih.gov/29156634/.
20. Lim, M. C.; Lee, G. H.; Huynh, D. T. N.; Letona, C. A. M.; Seo, D. H.; Park, C. S.; Kim, Y. R. Amylosucrase-mediated synthesis and self-assembly of amylose magnetic microparticles. *RSC Adv.* **2015**, *5*, 36088-36091, https://doi.org/10.1039/C5RA02284C.
21. Wang, Y.; Li, L.; Luo, C.; Wang, X.; Duan, H. Removal of Pb_{2+} from water environment using a novel magnetic chitosan/graphene oxide imprinted Pb_{2+}. *Int. J. Biol. Macromol.* **2016**, *86*, 505-511, https://doi.org/10.1016/j.ijbiomac.2016.01.035.
22. Jaime, J.; Rangel, G.; Muñoz-Bonilla, A.; Mayoral, A.; Herrasti, P. Magnetite as a platform material in the detection of glucose, ethanol and cholesterol. *Sens. Actuators B Chem.* **2017,** *238*, 693-701, http://dx.doi.org/10.1016%2Fj.snb.2016.07.059.
23. Gregorio-Jauregui, K. M.; Pineda, M.; Rivera-Salinas, J. E.; Hurtado, G.; Saade, H.; Martinez, J. L.; López, R. G. One-step method for preparation of magnetic nanoparticles coated with chitosan. *J. Nanomater.* **2012**, *2012*, 1-9, https://www.hindawi.com/journals/jnm/2012/813958/.
24. Yallapu, M. M.; Othman, S. F.; Curtis, E. T.; Gupta, B. K.; Jaggi, M.; Chauhan, S. C. Multi-functional magnetic nanoparticles for magnetic resonance imaging and cancer therapy. *Biomaterials*. **2011**, *32*, PP. 1890-1905, https://doi.org/10.1016/j.biomaterials.2010.11.028.
25. Shalali, F.; Cheraghi, S.; Taher, M. A.; A sensitive electrochemical sensor amplified with ionic liquid and N-CQD/Fe3O4 nanoparticles for detection of raloxifene in the presence of tamoxifen as two essentials anticancer drugs, *Materials Chemistry and Physics* **2022**, *278*, 125658, https://doi.org/10.1016/j.matchemphys.2021.125658.
26. Khan, A. A.; Danish, M.; Rubaiee, S.; Yahya; S. M.; Insight into the investigation of Fe_3O4/SiO_2 nanoparticles suspended aqueous nanofluids in hybrid photovoltaic/thermal system, Cleaner Engineering and Technology **2022**, *11* ,100572, https://doi.org/10.1016/j.clet.2022.100572.
27. Wang, L.; Fan, Y-J.; Sun, Y-T.; Magnetically recyclable Cu-BTC@Fe_3O_4-catalyzed synthesis of aryl α-chlorobenzyl ketones. *Mendeleev Communications* **2022**, *32*, 801-803, https://doi.org/10.1016/j.mencom.2022.11.031.
28. Wang, Y.; Sheng, L.; Zhang; X.; Li, J.; Wang, R.; Hybrid carbon molecular sieve membranes having ordered Fe_3O_4@ZIF-8-derived microporous structure for gas separation, *Journal of Membrane Science* **2023**, *666*, 121127, https://doi.org/10.1016/j.memsci.2022.121127.
29. Zhang, W.; Jia, S.; Wu, Q.; Wu, S.; Ran, J.; Liu, Y.; Hou, J. Studies of the magnetic field intensity on the synthesis of chitosan-coated magnetite nanocomposites by co-precipitation method. *Mater. Sci. Eng. C.* **2012,** *32*, 381-384, http://dx.doi.org/10.1016/j.msec.2011.11.010.
30. Shen, C.; Shen, Y.; Wen, Y.; Wang, H.; Liu, W. Fast and highly efficient removal of dyes under alkaline conditions using magnetic chitosan-Fe (III) hydrogel. *Water Res.* **2011**, *45*, 5200-5210, https://doi.org/10.1016/j.watres.2011.07.018.
31. Liandi, A. R.; Cahyana, A. H.; Yunarti, R. T.; Wendari, T. P. Facile synthesis of magnetic Fe3O4@Chitosan nanocomposite as environmentally green catalyst in multicomponent Knoevenagel-Michael domino reaction. *Ceram. Int.* **2022,** *48*, 20266-20274, https://doi.org/10.1016/j.ceramint.2022.03.307.
32. Roy, N.; Alex, S. A. Chandrasekaran, N., Kannabiran, K., Mukherjee, A. Studies on the removal of acid violet 7 dye from aqueous solutions by green ZnO@Fe_3O_4 chitosan–alginate nanocomposite synthesized using Camellia sinensis extract. *J. Environ. Manage.* **2021,** *303*, 0301-4797, https://doi.org/10.1016/j.jenvman.2021.114128.
33. Roy, N.; Kannabiran, K.; Mukherjee, A. Studies on photocatalytic removal of antibiotics, ciprofloxacin and sulfamethoxazole, by Fe_3O_4-ZnO-Chitosan/Alginate nanocomposite in aqueous systems. *Adv. Powder Technol.* **2022,** *33*, 103691, https://doi.org/10.1016/j.apt.2022.103691.
34. Bashir, S.; Teo, Y. Y.; Ramesh, S.; Ramesh, K.; Rizwan, M. Synthesis and characterization of PH-Sensitive N-Succinyl chitosan hydrogel and its properties for biomedical applications. *J. Chil. Chem. Soc.* **2019,** *64*, 4571-4574, http://dx.doi.org/10.4067/S0717-97072019000304571.
35. Braim, F. S.; Ashikin Nik Ab Razak, N. N.; Abdul Aziz, A.; Ismael, L. Q.; Sodipo, B. K. "Ultrasound assisted chitosan coated iron oxide nanoparticles: Influence of ultrasonic irradiation on the crystallinity, stability, toxicity and magnetization of the functionalized nanoparticles. *Ultrasonics Sonochemistry* **2022**, *8*, 106072, https://doi.org/10.1016/j.ultsonch.2022.106072.
36. Hassani, S.; Gharehaghaji, N.; Divband, B. Chitosan-coated iron oxide/graphene quantum dots as a potential multifunctional nanohybrid for bimodal magnetic resonance/fluorescence imaging and 5-fluorouracil delivery, *Materials today communications* **2022**, *7*, 103589, https://doi.org/10.1016/j.mtcomm.2022.103589.
37. Cai, Y.; Karmakar, B.; Salem, M. A.; Alzahrani, A. Y.; Bani-Fwaz, M. Z.; Oyouni, A. A. A.; Al-Amer, O.; Batiha, G. E. Ag NPs supported chitosan-agarose modified Fe_3O_4 nanocomposite catalyzed synthesis of

indazolo[2,1-b]phthalazines and anticancer studies against liver and lung cancer cells. *Int. J. Biol. Macromol.* **2022,** *208*, 20-28, https://doi.org/10.1016/j.ijbiomac.2022.02.172.
38. Liandi, A. R.; Cahyana, A. H.; Yunarti, R. T.; Wendari, T. P. Facile synthesis of magnetic Fe_3O_4@Chitosan nanocomposite as environmentally green catalyst in multicomponent Knoevenagel-Michael domino reaction. *Ceram. Int.* **2022**, *48*, 20266-20274, https://doi.org/10.1016/j.ceramint.2022.03.307.
39. Roy, N.; Kannabiran, K.; Mukherjee, A. Studies on photocatalytic removal of antibiotics, ciprofloxacin and sulfamethoxazole, by Fe_3O_4-ZnO-Chitosan/Alginate nanocomposite in aqueous systems. *Adv. Powder Technol.* **2022,** *33*, 103691, https://doi.org/10.1016/j.apt.2022.103691.
40. Kaveh, R.; Bagherzadeh, M. Simultaneous removal of mercury ions and cationic and anionic dyes from aqueous solution using epichlorohydrin cross-linked chitosan @ magnetic Fe_3O_4/activated carbon nanocomposite as an adsorbent. *Diam. Relat. Mater.* **2022,** *124*, 108923, https://doi.org/10.1016/j.diamond.2022.108923.
41. Fatema, N.; Sayed, M. G.; Asma, K. Bio-based Fe_3O_4/chitosan nanocomposite sensor for response surface methodology and sensitive determination of gallic acid,International *Journal of Biological Macromolecules* **2020**, *160*, 456-469, https://doi.org/10.1016/j.ijbiomac.2020.05.205.
42. Govindan, S.; Nivethaa, E. A. K.; Saravanan, R.; Narayanan, V.; Stephen, A. Synthesis and characterization of chitosan–silver nanocomposite. *Appl. Nanosci.* **2012,** *2*, 299-303, http://dx.doi.org/10.1007%2Fs13204-012-0109-5.
43. Rahman, N. A.; Abu Hanifah, S.; Mobarak, N. N.; Su'ait, M. S.; Ahmad, A.; Shyuan, L. K.; Khoon, L. T. Synthesis and characterizations of o-nitrochitosan based biopolymer electrolyte for electrochemical devices. *PloS. One.* **2019,** *14*, e0212066, https://doi.org/10.1371/journal.pone.0212066.
44. Jamshidiyan, M.; Shirani, A. S.; Alahyarizadeh, G. Solvothermal synthesis and characterization of magnetic Fe3O4 nanoparticle by different sodium salt sources. *Mater. Sci. -Pol.* **2017,** *35*, 50-57, https://doi.org/10.1515/msp-2017-0004.
45. Kyzas, G. Z.; Travlou, N. A.; Kalogirou, O.; Deliyanni, E. A. Magnetic graphene oxide: effect of preparation route on reactive black 5 adsorption. *Materials.* **2013,** *6*, 1360-1376. http://dx.doi.org/10.3390/ma6041360.
46. Patterson, A. L. The Scherrer formula for X-ray particle size determination. *Phys. Rev.* **1939,** *56*, 978-982, https://doi.org/10.1103/PhysRev.56.978.
47. Kefeni, K. K.; Msagati, T. A. M.; Mamba, B. B. Spinel ferrite nanoparticles: synthesis, characterisation and applications in electronic device. *Mater. Sci. Eng. B.* **2017,** *215*, 37–55, http://dx.doi.org/10.1007/978-3-319-56422-7_22.
48. Fernandes Queiroz, M.; Melo, K. R. T.; Sabry, D. A.; Sassaki, G. L.; Rocha, H. A. O. Does the use of chitosan contribute to oxalate kidney stone formation?. *Marine Drugs.* **2015,** *13*, 141-158, https://doi.org/10.3390%2Fmd13010141.
49. Gutha, Y.; Pathak, J. L.; Zhang, W., Zhang, Y.; Jiao, X. Antibacterial and wound healing properties of chitosan/poly (vinyl alcohol)/zinc oxide beads (CS/PVA/ZnO). *Int. J. Biol. Macromol.* **2017,** *103*, 234-24, https://doi.org/10.1016/j.ijbiomac.2017.05.020.
50. Soundarrajan, M.; Gomathi, T.; Sudha, P. N. Understanding the adsorption efficiency of chitosan coated carbon on heavy metal removal. *Int. J. Sci. Res. Publ*. **2013,** *3*, 1-10.
51. Yang, L.; Tian, J., Meng, J.; Zhao, R.; Li, C., Ma, J.; Jin, T. Modification and characterization of Fe_3O_4 nanoparticles for use in adsorption of alkaloids. *Molecules* **2018,** *23*, 562, https://doi.org/10.3390%2Fmolecules23030562.
52. Aziz, S. B.; Abdulwahid, R. T.; Rasheed, M. A.; Abdullah, O. G.; Ahmed, H. M. Polymer blending as a novel approach for tuning the SPR peaks of silver nanoparticles. *Polymers* **2017,** *9*, 486, https://doi.org/10.3390%2Fpolym9100486.
53. Deghiedy, N. M.; El-Sayed, S. M. Evaluation of the structural and optical characters of PVA/PVP blended films. *Optical Materials* **2020,** *100*, 109667, https://doi.org/10.1016/j.optmat.2020.109667.
54. Soliman, T. S.; Vshivkov, S. A. Effect of Fe nanoparticles on the structure and optical properties of polyvinyl alcohol nanocomposite films. *J. Non-Cryst. Solids* **2019,** *519*, 119452, https://doi.org/10.1016/j.jnoncrysol.2019.05.028.
55. Mott, N. F.; Davis, E. A. Electronic processes in non-crystalline materials, Oxford, 2nd edn. Clarendon, **1979**.
56. Deng, Z. J.; Mortimer, G.; Schiller, T.; Musumeci, A.; Martin, D.; & Minchin, R. F. Differential plasma protein binding to metal oxide nanoparticles. *Nanotechnology* **2009,** *20*, 455101, https://doi.org/10.1088/0957-4484/20/45/455101.
57. Teske, S. S.; Detweiler, C. S. The biomechanisms of metal and metal-oxide nanoparticles' interactions with cells. *Int. J.* Environ. Res. *Public Health* **2015,** *12*, 1112-1134, https://doi.org/10.3390%2Fijerph120201112.